ORIGINAL PAPER

Thermal conductivity of silicon and carbon hybrid monolayers: a molecular dynamics study

Lin Wang · Huai Sun

Abstract Thermal conductivities of graphene-like silicon and carbon hybrid nanostructures with silicon atom percentages varying from 0 % (graphene) to 100 % (silicene) are investigated using the reserve non-equilibrium molecular dynamic (RNEMD) method and Tersoff bond order potentials. The thermal conductivity of graphene is dramatically reduced with increasing silicon concentration, and the reduction appears to be related more to the topological structures formed than the amount of doped silicon atoms present. The reduction is collectively contributed to by reduced phonon group velocities (v), phonon free paths (l_∞), and the specific heat capacity (c) of the material. For systems with high symmetry, thermal conductivity is mainly influenced by v and c. For systems with low symmetry, thermal conductivity is dominated by l_∞; such materials are also more direction-dependent on thermal flux than highly symmetric materials.

Keywords Graphene · Molecular dynamics · Phonon · Silicon carbon hybrid monolayer · Thermal conductivity

Introduction

Graphene [1–10] may be modified to achieve different properties by the introduction of hybrid atoms or functional

L. Wang · H. Sun (✉)
School of Chemistry and Chemical Engineering & Key Laboratory
for Thin Film and Microfabrication of Ministry of Education,
Shanghai Jiao Tong University,
Shanghai 200240, China
e-mail: huaisun@sjtu.edu.cn

groups [11–13]. For instance, doping nitrogen on graphene results in increased electrocatalytic activity [14]. Experimental studies also show that band-gap openings in graphene may be induced by adsorption of atomic hydrogen [15]. Theoretical studies show that the thermal conductivity of hydrogenated graphene decreases with increasing hydrogen coverage [16, 17]. The synthesis of multi-walled Si-C nanotubes (SiCNTs) has recently been reported [18]. Although a graphene-like Si-C material has yet to be reported, DFT [19] and GTBMD [20] studies suggest that it may exist and it could be nonmagnetic with a wide band-gap semiconductor [21]. If all carbon atoms are replaced by silicon, a graphene-like all-silicon material (silicene) may be formed [22]. Very recently, silicon nanoribbons with a honeycomb graphene-like structure were synthesized by self-alignment on a Ag(110) surface [23]. Theoretical studies indicate that this kind of material has noticeable electronic poperties and may have potentially interesting electronic applications [24, 25].

Among the intriguing properties of graphene observed, its thermal conductivity has received significant attention from many researchers. Experimental and theoretical studies reveal that graphene has a superior thermal conductivity in the range of 2000 W/mK to 5000 W/mK [4, 5, 10], which provides various possibilities in the thermal management of nanoscale materials. Therefore, determination of changes in thermal conductivity as various amounts of silicon are doped on graphene is an interesting endeavor. The information obtained from such a study would be valuable for designing hybrid materials for thermal management.

In this work, we calculated the thermal conductivities of single-layer graphene (SLG), silicene (SLS), and silicon-carbon hybrid sheets with various percentages of silicon atoms (SLSiC). Calculations were based on the reverse non-equilibrium molecular dynamics (RNEMD) method [26] and Tersoff bond-order potentials [27]. We also compared

different compositions and thermal flux directions in the proposed materials. Finally, we carried out phonon dispersion calculations and interpreted the calculated data using thermal conductivity kinetic models to better understand the physical origins of the data obtained. This article summarizes our studies.

Computational details

Figure 1 illustrates the single layer models calculated in this work. A total of 12 structures were calculated, with different mole fractions of silicon atoms: 0 (SLG), 1/96, 1/12, 1/6, 1/4, 1/3, 1/2, and 1 (SLS). The models in this paper were named by the silicon ratio and type of topological structure presented. For example, Si-1/2-I denotes a structure with 1/2 silicon atoms and type I topology. Two directions, armchair (AC) and zigzag (ZZ), were also defined for the models, as illustrated in Fig. 1. We selected these structures for the following reasons: (1) Structures 1 to 8 were selected to determine the variation in thermal conductivity as the silicon atom percentage increased. Silicon atoms were evenly distributed in these structures along the AC direction. (2) Structures 1 and 7 to 9

Fig. 1 Models calculated in this work. The displayed models are NOT optimized for clear viewing. Black: carbon; yellow: silicon
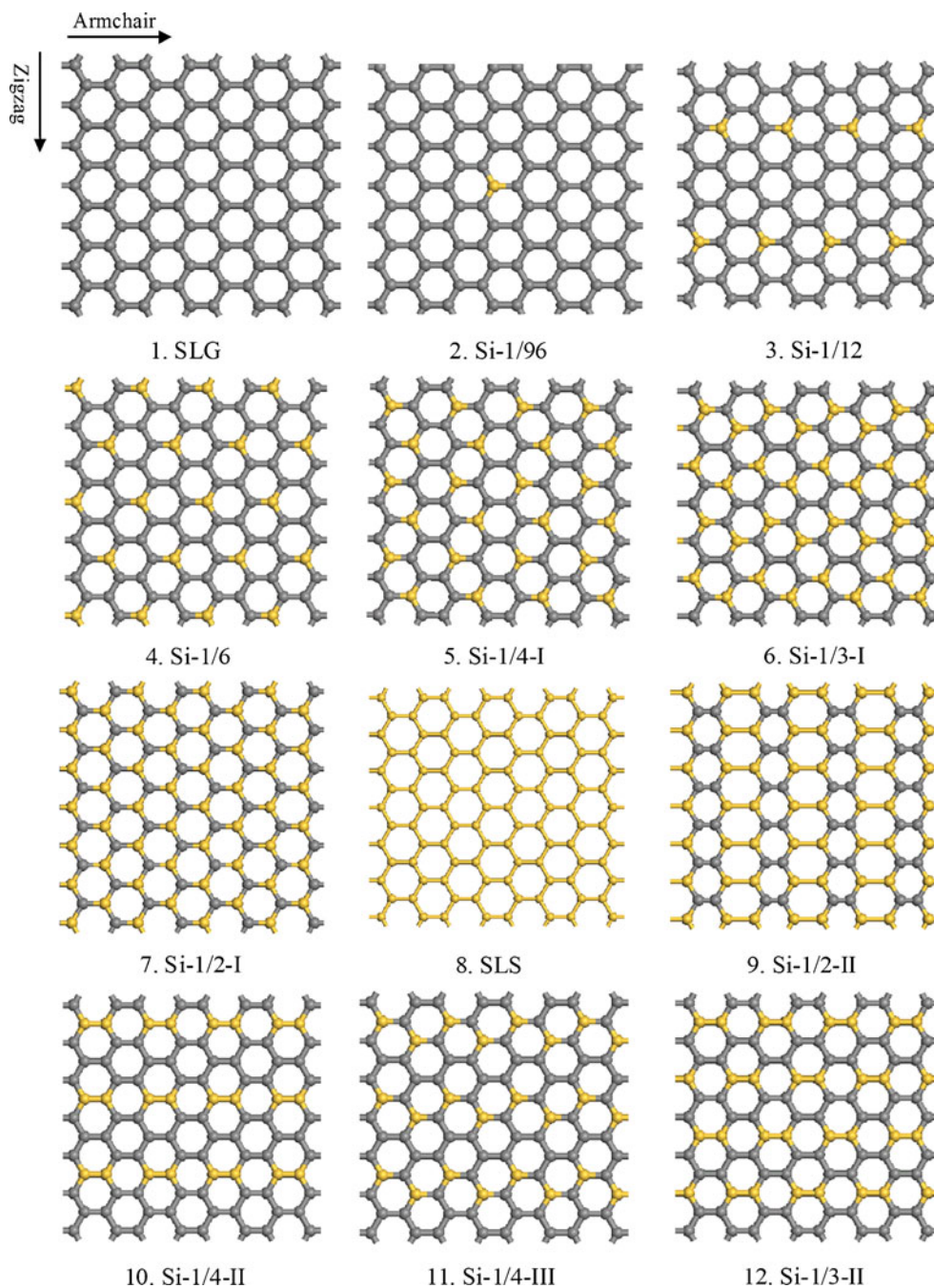
were selected to determine the effects of direction on the calculated thermal conductivities. In structure 9, Si-1/2-II, for example, four directions were defined and calculated. (3) Structures 9 to 12 were used to compare the effects of different topologies as structures with same carbon-silicon ratios but different topologies included in group (1). In particular, structures 9, 10, and 12 contain Si–Si bonds, which have been reported to be less stable than alternating Si–C bonds by theoretical studies [19, 20].

Simulations were performed using 3-D periodic conditions, in which a single layer was placed on the x-y plane. A large separation (>2.0 nm) in the z-direction was used to avoid interactions between real and imaginary layers of the simulation cell. The y-dimension varied between 1.5 nm and 2.6 nm depending on the fraction of silicon in the model; the number of atoms along the y-dimension was kept fixed. The x-dimension was chosen as the direction of heat flux in RNEMD simulations. Extrapolations were performed using simulations on super-cells made by duplicating the x-axis such that it spanned 30 nm to 90 nm to reduce simulation size effects.

In the RNEMD simulations, each of the simulation boxes was divided into 20 blocks along the x-dimension. The 1st block was treated as the cold region and the 11th block was treated as the hot region. The temperature gradient was generated by repeatedly swapping velocities of atoms between the cold and hot regions during otherwise regular molecular dynamics simulations. As the system reached equilibrium, the temperature gradient ($\partial T / \partial x$) and heat flux (J) calculated from the exchanged kinetic energies per unit time and cross-area were collected. The thermal conductivity was calculated as:

$$\kappa = -\frac{J}{\langle \partial T / \partial x \rangle} = -\frac{\sum_{i=1}^{n} \frac{1}{2} m_i \left(v_{hi}^2 - v_{ci}^2 \right)}{2At\langle \partial T / \partial x \rangle}. \tag{1}$$

In the equation, m_i is the mass of the atoms, v_{hi} and v_{ci} are velocities in the hot and cold regions, respectively, A is the cross-area, and t is the total simulation time. Thicknesses of 0.34 nm for SLG and 0.42 nm for all other models containing silicon were used to calculate the cross area. The factor of 2 accounted for energy flows from hot to cold regions in two directions due to periodic setups along the x-direction.

The simulations were performed with the LAMMPS package [28] and Tersoff bond-order potentials [27] at room temperature. A time step of 0.25 fs was used for the molecular dynamics simulations. The initial structures were equilibrated by NPT simulation for 100 ps, followed by NVT simulation for another 100 ps. The data collection period was typically 1.0 ns, and the interval of collection was 25 fs; data collected were used to calculate the temperature gradient. The frequency of velocity swaps between hot and cold regions was

adjusted to keep the temperature of the simulation box between 250 and 350 K. Phonon dispersion curves were calculated using the software package GULP [29].

Results and discussion

Figure 2 shows the temperature profile and extrapolation chart obtained for SLG. Extrapolation data obtained for other models are similar and given in the supplementary material (S1). The temperature profile shown in Fig. 2a does not show perfect linearity in the vicinities of hot or cold boundaries. Similar results were obtained for other models in this work. The lack of perfect linearity is due to the scattering of phonons in temperature-controlled blocks and often observed in NEMD simulations of systems with high
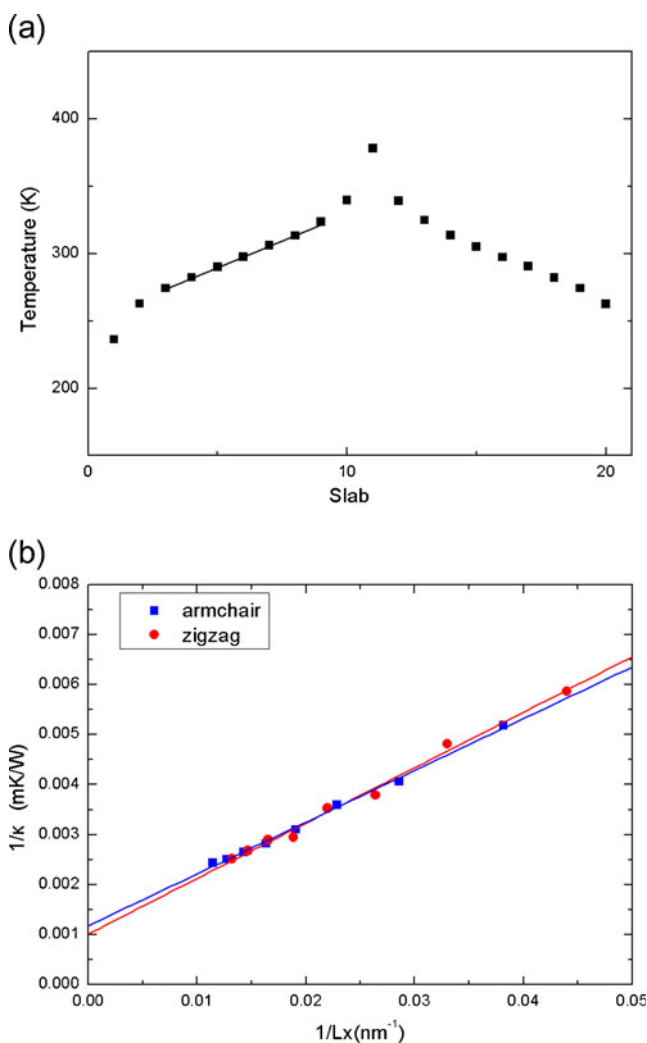

Fig. 2 (a) Final temperature profile of 87.3 nm long graphene at room temperature. (b) The linear response between the reciprocal of thermal conductivity and the reciprocal of the simulation box length of SLG along different directions at room temperature. Square: armchair; circle: zigzag

thermal conductivity [30]. Linear regions can be identified in the heat spread blocks (blocks 3 to 9), which are used to calculate temperature gradients.

The calculated thermal conductivity coefficients depend on the simulation box lengths. Finite lengths used in the simulations can be removed by extrapolation. The lattice thermal conductivity can be described by the following kinetic formula [31]:

$$\kappa = \frac{1}{3}cvl, \qquad (2)$$

where c is the specific heat capacity, v is the average phonon group velocity, and l is the phonon mean free-path. The mean free-path can be divided to two parts based on the Matthiessen rule [32]:

$$\frac{1}{l} = \frac{1}{l_\infty} + \frac{2}{L_X}, \qquad (3)$$

where L_x is the finite length along the thermal flux direction in the simulation box and l_∞ is the phonon mean free path in an infinitely long (real) system. The factor 2 accounts for the fact that phonon scattering occurs in the heat sink and source regions, as well as at both boundaries of the simulation box. Combining Eqs. 2 and 3, we obtain an extrapolation formula as follows:

$$\frac{1}{\kappa} = \frac{3}{cv}\left(\frac{1}{l_\infty} + \frac{2}{L_X}\right) = A + \frac{B}{L_X}. \qquad (4)$$

The reciprocal of the calculated thermal conductivities is a linear equation of the reciprocal of the x-dimension lengths, with the intercept being the thermal conductivity at infinite conditions:

$$A = \frac{1}{\kappa_\infty} = \frac{3}{cvl_\infty} \qquad (5)$$

l_∞ can be calculated from constants A and B [33]:

$$l_\infty = \frac{B}{2A}. \qquad (6)$$

The extrapolation for SLG is displayed in Fig. 2b. For SLG, calculations are carried out along two directions: AC and ZZ. Each of the data sets can be reasonably fit by a straight line. The extrapolated conductivity values are 848 W/m-K for AC and 986 W/m-K for ZZ, significantly lower than reported experimental data (~3080-5300 W/mK) [4, 5] but close to previously published simulation results (~1200 W/mK for AC and ~1600 W/mK for ZZ) obtained using different potentials [9]. The potential is undoubtedly one of the major factors that influences the predictions. The calculated phonon density of state, as given in the supplementary material (S2), shows that

calculated frequencies using Tersoff potentials are significantly higher than the experimental data [34]. The discrepancy uncovered may be attributed to the ineffectiveness of the underlying potential; further investigation of this subject is necessary to achieve more concrete conclusions.

Figure 3 summarizes the calculated thermal conductivities as the mole fraction of silicon atoms in both the AC and ZZ directions. Similar results are obtained for the two directions, although ZZ values are slightly higher than AC ones in most cases. A very small fraction (1/96) of silicon causes a dramatic decrease in thermal conductivity from (850 to 1000) W/mK to (130 to 140) W/mK. As the fraction of silicon increases, the values decrease rapidly to as low as ca. 10 W/mK for silicon fractions of 1/12, 1/6, 1/4, and 1/3. However, thermal conductivities are modest in 1/2 silicon and all silicon (SLS) models, approximating 110 W/mK and 55 W/mK, respectively.

Analysis of the SLG, Si-1/2-I, and SLS models, which have relatively large thermal conductivities, reveals the physical origin of the coefficients of thermal conductivity. These models have similar topological structures and each model contains only one of the three chemical bonds: C–C, C–Si, or Si–Si. Table 1 lists a comparison of calculated results for SLG, Si-1/2-I, and SLS along the ZZ and AC directions. The calculated cv and l_∞, based on extrapolation of Eqs. 3 to 6 are also listed in the table. It is clear that the decrease in thermal conductivity from SLG to SLS is mainly due to the decrease in cv, while l_∞ is only reduced fractionally.

A comparison of the data obtained for different directions (AC and ZZ) in Table 1 shows that the thermal conductivity increases from 848 W/mK to 986 W/mK for SLG and 101 W/mK to 118 W/mK for Si-1/2-I and remains almost identical for SLS. The calculated l_∞ shows that the ZZ direction has a larger l_∞ than the AC direction. This finding
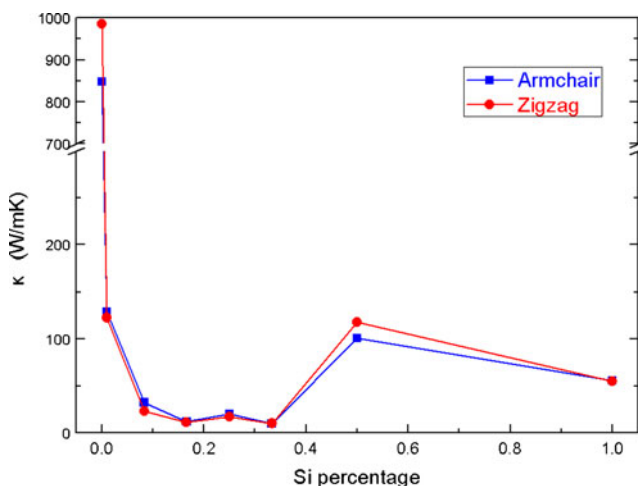

Fig. 3 Variation in thermal conductivity with the percentage of doped silicon in the armchair and zigzag directions

Table 1 Calculated thermal conductivities κ (W/mK) from the combined contributions of cv (10^9 W/m^{2}K) and phonon mean free path l_∞ (nm) for the highly symmetrical materials SLG, Si-1/2-I, and SLS. The experimental thermal conductivities of SLG are retrieved from Ghosh et al. [4, 5]

	AC			ZZ			experiment
	κ	cv	l_∞	κ	cv	l_∞	κ
SLG	848.1	57.9	43.9	985.9	54.1	54.6	3080-5300
Si-1/2-I	101.1	7.5	40.2	117.6	6.1	57.1	
SLS	55.6	5.2	32.0	54.9	5.1	31.8	

is consistent with a recent study by Jiang et al. [35] on graphene thermal conductivity.

The collective contribution of cv can be further decoupled by estimating v and c. To estimate v, we calculate phonon dispersion curves for these models along the highly symmetrical direction (Γ-M-K-Γ), the results of which are plotted in Fig. 4. The group velocity can be estimated as the slope of the phonon curve at the Γ point. Since the thermal conductivity is dominated by contributions of the acoustic modes [36, 37], we calculate the slopes of the three acoustic modes (LA, TA, ZA) only and list the results in Table 2. The v values, which are obtained by averaging the three branches [30], are also given in the table. Values of v decrease in the order of SLG > Si-1/2-I > SLS. However, the extent of reduction in v is not identical to that of the combined value cv, which means c also partly contributes to the results obtained.

Accurate calculations of c are beyond the scope of this work; however, we can obtain a very rough estimate of the magnitudes of change based on the equal partition theorem [30]:

$$c = \frac{3}{2}k_B N, \tag{7}$$

where N is the number density, which are 107 nm^{-3} for SLG, 56 nm^{-3} for Si-1/2-I, and 35 nm^{-3} for SLS. Clearly, both v and c are reduced as the fraction of silicon atoms increases in the three models.

Model Si-1/2-II is ideal for analyzing the direction of heat fluxes. Four distinct directions can be identified for this model as shown in Fig. 5. In addition to ZZ (I) and AC (IV), directions II and III are not found in models SLG, SLS and Si-1/2-I. The calculated thermal conductivities and their components in terms of cv and l_∞ are listed in Table 3. The data obtained for direction ZZ is very similar to that obtained for Si-1/2-I (ZZ). This can be justified by comparing the structures (Fig. 1); along the ZZ direction, both materials show the same zigzagging C–Si–C–Si bond structure. The value along the AC direction is, however, very different from that of Si-1/2-I. As shown in Fig. 1, the bond pattern is C–C–Si–Si in SiC-1/2-II but is C–Si–C–Si in SiC-
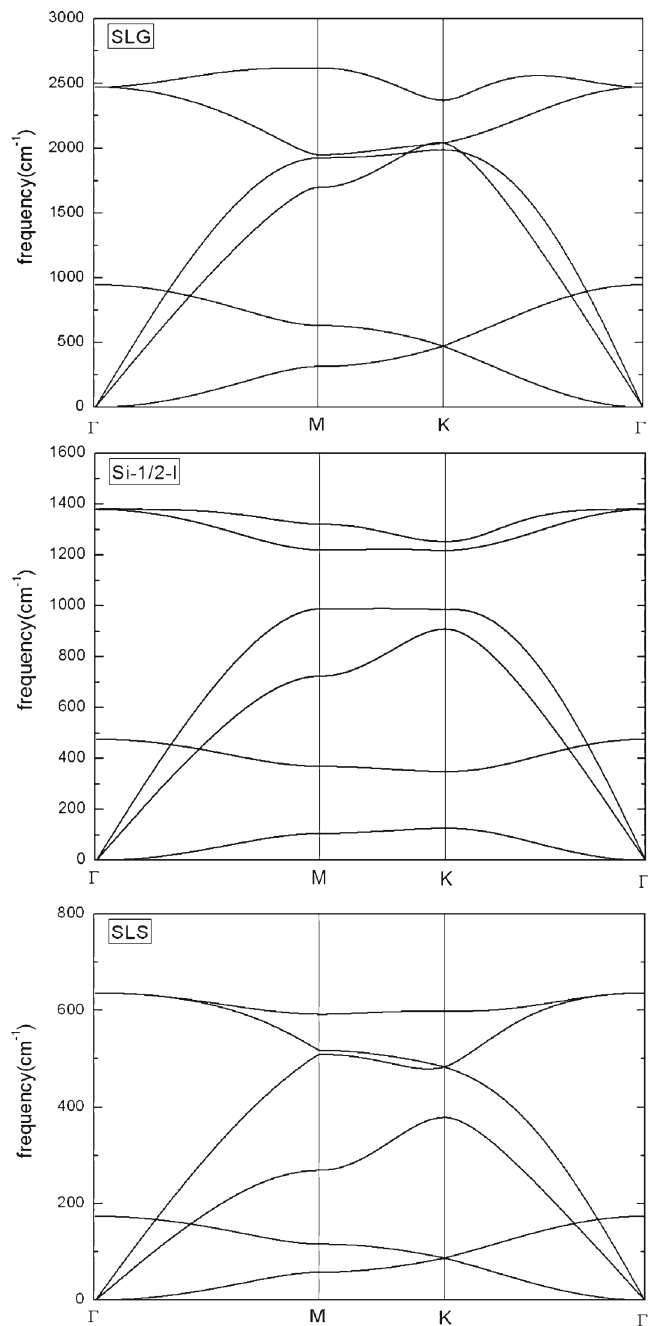

Fig. 4 The calculated phonon dispersion curves along high-symmetry directions Γ-M-K-Γ for different materials

Table 2 Calculated phonon velocities (km/s) of acoustic modes (LA, TA, ZA) around the Γ point and average phonon velocities for different materials

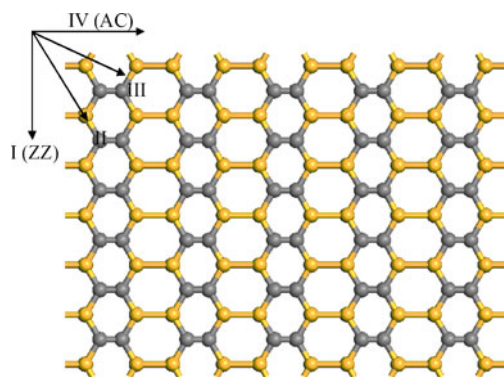|	v_{LA}	v_{TA}	v_{ZA}	v
SLG	50.3	36.8	1.6	41.3
Si-1/2-I	19.5	13.9	0.50	15.8
SLS	6.8	4.2	0.18	5.1

Fig. 5 The effect of thermal flux directions in Si-1/2-II. The arrow indicates directions of thermal flux used to calculate thermal conductivities

1/2-I. This difference in pattern leads to large differences in calculated thermal conductivity: 47.5 W/mK for SiC-1/2-II and 101.1 W/mK for SiC-1/2-II. We note that the differences may be attributed to both the product of cv (1.9 vs. 7.5) and the l_∞ (71.8 vs. 40.2). Directions II and III are similar but distinguishable in terms of thermal conductivities, the products of cv and l_∞. Models Si-1/2-I and Si-1/2-II have the same composition but different topological structures and symmetries. Generally speaking, as the symmetry is reduced (such as from Si-1/2-I to Si-1/2-II, the space group number of operators is reduced from 12 to 8), the direction-dependence of thermal conductivity increases.

Table 4 lists results for models with very low thermal conductivity. In Si-1/96, doping with only 1 % silicon causes a dramatic decrease in thermal conductivity from 848 W/mK to 143 W/mK. As the percentage of silicon increases, the thermal conductivities decrease rapidly to ca. 10 W/mK; these values are lower than that of pure silicon (SLS). As discussed above, once silicon is added to graphene, both v and c are reduced. This is clear in Table 4, which shows that most of the cv values are less than 10. Comparing the Si-1/2 and SLS models, remarkable reductions in l_∞ are observed.

Surface structures are important factors corresponding to the thermal conductivities calculated. Figure 6 displays snapshots of structures obtained from the simulations. Figure 6a displays the structure obtained for the Si-1/96

Table 4 Calculated thermal conductivities along the AC direction κ (W/mK) from the combined contributions of cv (10^9 W/m^{2}K) and phonon mean free path l_∞ (nm) for different materials

ID	κ	cv	l_∞
Si-1/96	143.4	19.5	22.0
Si-1/12	32.1	9.6	9.9
Si-1/6	11.8	9.2	3.8
Si-1/4-I	19.8	4.5	13.1
Si-1/4-II	8.2	16.8	1.4
Si-1/4-III	5.7	6.5	2.6
Si-1/3-I	9.9	9.3	3.1
Si-1/3-II	10.0	13.4	2.2

model. The silicon atom is surrounded by carbon atoms. As Si–C bonds are longer than C–C bonds, silicon atoms become puckered out of the graphene plane by ∼0.16 nm. These atoms contribute to impurities or defects on the surface of the material, causing strong phonon scattering and decreasing l_∞ compared with SLG. Similar phenomena were observed for the Si-1/12 model. Structures of Si-1/6, Si-1/4-(I, II, III) and Si-1/3-(I, II) possess alternating C–C, C–Si, or Si–Si bonds, showing wavelike or rippled surface features. Figure 6b shows the structure of Si-1/3-I as an example. Comparison of the various silicon structures indicates that the rougher the surface becomes, the shorter l_∞ is. Figure 6c shows a snapshot of the model of Si-1/2-I. A planar structure is obtained for this model, which agrees with DFT calculations [16]; a modest value of thermal conductivity is also obtained. Overall, the smoother a surface is, the greater its thermal conductivity becomes.

Conclusions

To summarize, thermal conductivities of graphene-like silicon and carbon hybrid nanostructures with silicon atom percentages varying from 0 % (graphene) to 100 % (silicene) were investigated using the reserve non-equilibrium
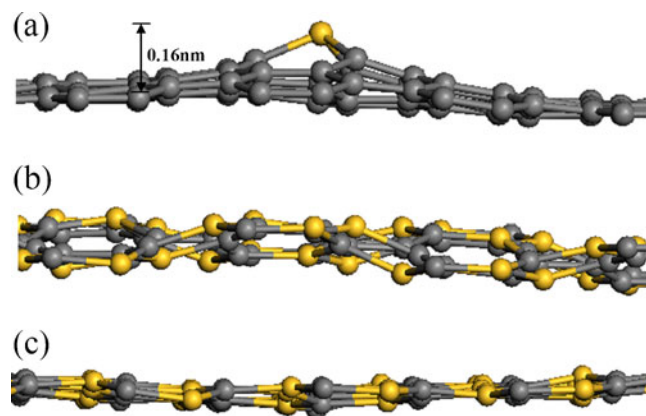
Table 3 Calculated thermal conductivities κ (W/mK) from the combined contributions of cv (10^9 W/m^{2}K) and phonon mean free path l_∞ (nm) for different thermal flux directions in Si-1/2-II

	κ	cv	l_∞
I (ZZ)	111.5	6.3	52.7
II	66.1	7.7	25.6
III	53.7	4.1	39.1
IV(AC)	47.5	1.9	71.8

Fig. 6 Snapshots of structures during molecular dynamics simulations: (**a**) Si-1/96, (**b**) Si-1/3-I, and (**c**) Si-1/2-I

molecular dynamic (RNEMD) method and Tersoff bond order potentials. The finite boundary condition effect was effectively removed by extrapolation. Using data calculated for SLG, we observed that the calculated thermal conductivity was significantly lower than the experimental data but consistent with previously reported calculation data. The discrepancy uncovered may be attributed to the ineffectiveness of the underlying potential; further investigation of this subject is necessary to achieve more concrete conclusions.

The simulation data showed that thermal conductivities decreased dramatically as silicon was doped on graphene. However, this decrease was not proportional to the amount of silicon added: even doping with 1 % silicon caused a dramatic decrease in thermal conductivity. Topological structures strongly influenced the thermal conductivity and direction-dependence of such conductivity. Anisotropic thermal conductivity is more pronounced for materials with low symmetry than those with high symmetry.

The calculated data were analyzed based on phonon dispersion curves and kinetic models in terms of c, v, and l_∞. The reduction in thermal conductivity with doped silicon was caused by the collective effects of three variables. For highly symmetrical models (i.e., SLG, Si-1/2-I and SLS), thermal conductivities were mainly determined by c and v. For low-symmetry models, l_∞ was the main cause of the reduction in thermal conductivity, indicating increased phonon scattering.

The results suggest that the thermal conductivity of silicon and carbon hybrid graphene-like materials imposes a large range of thermal conductivities depending on the amount of silicon doping and direction of heat flux, which could be useful for future applications in advanced thermal management.

References

1. Novoselov KS, Geim AK, Morozov SV, Jiang D, Zhang Y, Dubonos SV, Grigorieva IV, Firsov AA (2004) Electric field effect in atomically thin carbon films. Science 306:666–669. doi:10.1126/science.1102896
2. Novoselov KS, Geim AK, Morozov SV, Jiang D, Katsnelson MI, Grigorieva IV, Dubonos SV, Firsov AA (2005) Two-dimensional gas of massless dirac fermions in graphene. Nature 438:197–200. doi:10.1038/nature04233
3. Morozov SV, Novoselov KS, Katsnelson MI, Schedin F, Ponomarenko LA, Jiang D, Geim AK (2006) Strong suppression of weak localization in graphene. Phys Rev Lett 97:016801. doi:10.1103/PhysRevLett.97.016801
4. Balandin AA, Ghosh S, Bao WZ, Calizo I, Teweldebrhan D, Miao F, Lau CN (2008) Superior thermal conductivity of single-layer graphene. Nano Lett 8:902–907. doi:10.1021/nl0731872

5. Ghosh S, Calizo I, Teweldebrhan D, Pokatilov EP, Nika DL, Balandin AA, Bao WZ, Miao F, Lau CN (2008) Extremely high thermal conductivity of graphene: Prospects for thermal management applications in nanoelectronic circuits. Appl Phys Lett 92:151911. doi:10.1063/1.2907977
6. Patil AJ, Vickery JL, Scott TB, Mann S (2009) Aqueous stabilization and self-assembly of graphene sheets into layered bio-nanocomposites using DNA. Adv Mater 21:3159–3164. doi:10.1002/adma.200803633
7. Lu CH, Yang HH, Zhu CL, Chen X, Chen GN (2009) A graphene platform for sensing biomolecules. Angew Chem Int Ed 48:4785–4787. doi:10.1002/anie.200901479
8. Stampfer C, Schurtenberger E, Molitor F, Güttinger J, Ihn T, Ensslin K (2008) Tunable graphene single electron transistor. Nano Lett 8:2378–2383. doi:10.1021/nl801225h
9. Gunlycke D, Areshkin DA, Li J, Mintmire JW, White CT (2007) Graphene nanostrip digital memory device. Nano Lett 7:3608–3611. doi:10.1021/nl0717917
10. Hu JN, Ruan XL, Chen YP (2009) Thermal conductivity and thermal rectification in graphene nanoribbons: a molecular dynamics study. Nano Lett 9:2730–2735. doi:10.1021/nl901231s
11. Liu L, Ryu SM, Tomasik MR, Stolyarova E, Jung N, Hybertsen MS, Steigerwald ML, Brus LE, Flynn GW (2008) Graphene oxidation: thickness-dependent etching and strong chemical doping. Nano Lett 8:1965–1970. doi:10.1021/nl0808684
12. Wang Y, Shao YY, Matson DW, Li JH, Lin YH (2010) Nitrogen-doped graphene and its application in electrochemical biosensing. ACS Nano 4:1790–1798. doi:10.1021/nn100315s
13. Jang JW, Lee CE, Lyu SC, Lee TJ, Lee CJ (2004) Structural study of nitrogen-doping effects in bamboo-shaped multiwalled carbon nanotubes. Appl Phys Lett 84:2877–2879. doi:10.1063/1.1697624
14. Qu L, Liu Y, Baek JB, Dai LM (2010) Nitrogen-doped graphene as efficient metal-free electrocatalyst for oxygen reduction in fuel cells. ACS Nano 4:1321–1326. doi:10.1021/nn901850u
15. Balog R, Jorgensen B, Nilsson L, Andersen M, Rienks E, Bianchi M, Fanetti M, Lagsgaard E, Baraldi A, Lizzit S, Sljivancanin Z, Besenbacher F, Hammer B, Pedersen TG, Hofmann P, Hornekar L (2010) Bandgap opening in graphene induced by patterned hydrogen adsorption. Nat Mater 9:315–319. doi:10.1038/nmat2710
16. Pei QX, Sha ZD, Zhang YW (2011) A theoretical analysis of the thermal conductivity of hydrogenated graphene. Carbon 49:4752–4759. doi:10.1016/j.carbon.2011.06.083
17. Chien SK, Yang YT, Chen CK (2011) Influence of hydorgen functionalization on thermal conductivity of graphene: nonequilibrium molecular dynamics simulations. Appl Phys Lett 98:033107. doi:10.1063/1.3543622
18. Sun XH, Li CP, Wong WK, Wong NB, Lee CS, Lee ST, Teo BK (2002) Formation of silicon carbide nanotubes and nanowires via reaction of silicon (from disproportionation of silicon monoxide) with carbon nanotubes. J Am Chem Soc 124:14464–14471. doi:10.1021/ja0273997
19. Huda MN, Yan YF, Al-Jassim MM (2009) On the existence of Si-C double bonded graphene-like layers. Chem Phys Lett 479:255–258. doi:10.1016/j.cplett.2009.08.028
20. Menon M, Richter E, Mavrandonakis A, Froudakis G, Andriotis AN (2004) Structure and stability of SiC nanotubes. Phys Rev B 69:115322. doi:10.1103/PhysRevB.69.115322
21. Bekaroglu E, Topsakal M, Cahangirov S, Ciraci S (2010) First-principles study of defects and adatoms in silicon carbide honeycomb structures. Phys Rev B 81:075433. doi:10.1103/PhysRevB.81.075433
22. Rao CNR, Sood AK, Subrahmanyam KS, Govindaraj A (2009) Graphene: the new two-dimensional nanomaterial. Angew Chem Int Ed 48:7752–7778. doi:10.1002/anie.200901678
23. Aufray B, Kara A, Vizzini S, Oughaddou H, Léandri C, Ealet B, Lay GL (2010) Plasmon modes of silver nanowire on a silica substrate. Appl Phys Lett 96:183102. doi:10.1063/1.3509415

24. Jose D, Datta A (2011) Structures and electronic properties of silicene clusters: a promising material for FET and hydrogen storage. Phys Chem Chem Phys 13:7304–7311. doi:10.1039/C0CP02580A

25. Houssa M, Scalise E, Sankaran K, Pourtois G, Afanas'ev VV, Stesmans A (2011) Electronic properties of hydrogenated silicene and germanene. Appl Phys Lett 98:223107. doi:10.1063/1.3595682

26. Müller-Plathe F (1997) A simple nonequilibrium molecular dynamics method for calculating the thermal conductivity. J Chem Phys 106:6082–6085. doi:10.1063/1.473271

27. Tersoff J (1989) Modeling solid-state chemistry: interatomic potentials for multicomponent systems. Phys Rev B 39:5566–5568. doi:10.1103/PhysRevB.39.5566

28. Plimpton SJ (1995) Fast parallel algorithms for short-range molecular dynamics. J Comp Phys 117:1–19. doi:10.1006/jcph.1995.1039

29. Gale JD, Rohl AL (2003) The general utility lattice program. Mol Simul 29:291–341. doi:10.1080/0892702031000104887

30. Schelling PK, Phillpot SR, Keblinski P (2002) Comparison of atomic-level simulation methods for computing thermal conductivity. Phys Rev B 65:144306. doi:10.1103/PhysRevB.65.144306

31. Ashcroft NW, Mermin ND (1976) Solid state physics. Saunders, Fort Worth

32. Landry ES, Hussein MI, McGaughey AJH (2008) Complex super-lattice unit cell designs for reduced thermal conductivity. Phys Rev B 77:184302. doi:10.1103/PhysRevB.77.184302

33. Jiang H, Myshakin EM, Jordan KD, Warzinski RP (2008) Thermal conducitvity of methane hydrate from experiment and molecular simulation. J Phys Chem B 112:10207–10216. doi:10.1021/jp074419o

34. Tewary VK, Yang B (2009) Parametric interatomic potential for graphene. Phys Rev B 79:075442. doi:10.1103/PhysRevB.79.075442

35. Jiang JW, Wang JS, Li BW (2009) Thermal conductance of graphene and dimerite. Phys Rev B 79:205418. doi:10.1103/PhysRevB.79.205418

36. Chen G (1998) Thermal conductivity and ballistic-phonon transport in the cross-plane direction of superlattices. Phys Rev B 57:14958–14973. doi:10.1103/PhysRevB.57.14958

37. Chen G (1997) Size and interface effect on thermal conductivity of superlattices and periodic thin-film structures. J Heat Trans 119:220–229. doi:10.1115/1.2824212